Tool for Tortuosity Estimation in Lithium Ion Battery Porous Electrodes

Martin Ebner[*,z] and Vanessa Wood[**]

Laboratory for Nanoelectronics, Department of Information Technology and Electrical Engineering, ETH Zurich, 8092 Zurich, Switzerland

We present an open source software application "*BruggemanEstimator*" that allows a user to estimate the tortuosity of a porous electrode. *BruggemanEstimator* determines the Bruggeman exponent based on the Differential Effective Medium approximation and as input requires only two microscope images: one of the top and one of a cross section through an electrode. These images, which can be easily acquired with a scanning electron or optical microscope, are used to extract a sampling of active particle shapes as well as the orientation of the particles within the electrode. We validate the accuracy of *BruggemanEstimator* by comparing the estimated Bruggeman exponents to values calculated by performing numerical diffusion simulations on three-dimensional microstructures obtained from tomographic techniques.

Tortuosity, τ, is a dimensionless quantity that describes the influence of the morphology of a porous electrode on its effective transport properties.[1] It is an important parameter in determining the performance of a lithium ion battery electrode. We can describe effective diffusion of lithium in the electrolyte filling the pore structure of the electrode as:

$$D_{eff} = \frac{\varepsilon}{\tau} D_0 \qquad [1]$$

where ε is the porosity, τ the tortuosity, and D_0 is the diffusion coefficient of lithium in the electrolyte.[a]

The concept of tortuosity can be understood as the square ratio of diffusion length, L', and geometric length, L (i.e. electrode thickness), sketched in Figure 1a:

$$\tau = \left(\frac{L'}{L}\right)^2 \qquad [2]$$

To arrive at this geometrical interpretation of tortuosity, we consider the following argument: The mean square displacement, $\langle r^2(t)\rangle$, of a diffusing species with diffusion coefficient D in a background medium is calculated in d dimensional space as a function of time t with the *Einstein-Smoluchowsky* equation:[2,3]

$$\langle r^2(t)\rangle = 2d \cdot D \cdot t \qquad [3]$$

Diffusion within a porous body can be treated either (1) in the porous picture, where the diffusion coefficient, corrected for the influence of porosity,[b] is $D = \varepsilon D_0$ and the diffusion length is $\sqrt{\langle r^2(t)\rangle} = L'$, or (2) in a homogenized picture where the diffusion coefficient is $D = \frac{\varepsilon}{\tau} D_0$ and the diffusion length is $\sqrt{\langle r^2(t)\rangle} = L$. Applying Eq. 3 to both notations yields the geometric definition of tortuosity:

$$\frac{L'^2}{L^2} = \frac{2d \cdot \varepsilon D_0 \cdot t}{2d \cdot \frac{\varepsilon}{\tau} D_0 \cdot t} = \tau \qquad [4]$$

We note that the definition of tortuosity is inconsistent across literature. Our definition of tortuosity is sometimes called the *tortuosity factor* and the term tortuosity is then used for the square root of this quantity.[4]

Tortuosity of porous electrodes has traditionally been difficult to assess.[1,5,6] Recently, advances in 3D visualization techniques have made it possible to quantify tortuosity of porous electrodes and use the observed trends to understand the performance limitations that stem from lithium ion battery microstructure.[7–9] These visualization techniques include X-ray tomographic microscopy, conducted both at synchrotron facilities (SRXTM) as well as on laboratory-scale systems,[7,10] or focused-ion beam scanning electron microscope (FIB/SEM) tomography.[8]

To calculate tortuosity, a sub-volume of a porous electrode is visualized and numerical diffusion simulations are performed.[7] These techniques that enable the direct visualization of the microstructure provide extensive insights into porous electrodes and the effect of their structure on battery performance. For example, it was possible to determine that active particle shape and orientation has the most important impact on electrode tortuosity.[9] In addition, such studies have raised the question what role inhomogeneity in electrode microstructure plays in the context of battery life-time and failure.[7,11]

However, methods to obtain quantitative microstructure representations are experimentally and computationally expensive. Furthermore, certain materials pose challenges for 3D imaging in terms of size and contrast. Therefore, we look for a method that can be used to estimate the tortuosity based on easily obtainable information such as particle shape and size distributions.

A simple, yet powerful, estimation for tortuosity is the *Bruggeman relation*:

$$\tau = \varepsilon^{-\alpha} \qquad [5]$$

where α is the *Bruggeman exponent*.[12] Knowledge of α makes it possible to predict tortuosity for a given porosity. One important outcome of previous tomography studies was the demonstration of the validity of the Bruggeman relationship for porous electrodes and that the active particles play the most important role in determining the Bruggeman exponent.[9,13]

We therefore turn to the origins of the Bruggeman relation, the Differential Effective Medium (DEM) approximation as a tool to predict the Bruggeman exponent based only on knowledge of the active particle shape and orientation. We present an open source software application "*BruggemanEstimator*" that allows a user to estimate the tortuosity of a porous electrode based on the DEM approximation.

---

*Electrochemical Society Student Member.
**Electrochemical Society Active Member.
zE-mail: mebner@ethz.ch

[a]Analogously, the effective conductivity of the electrolyte can be expressed as $\kappa_{eff} = \frac{\varepsilon}{\tau}\kappa_0$.
[b]This can be understood as the reduction in cross-section area: $\varepsilon = A_{pore}/A_0$.
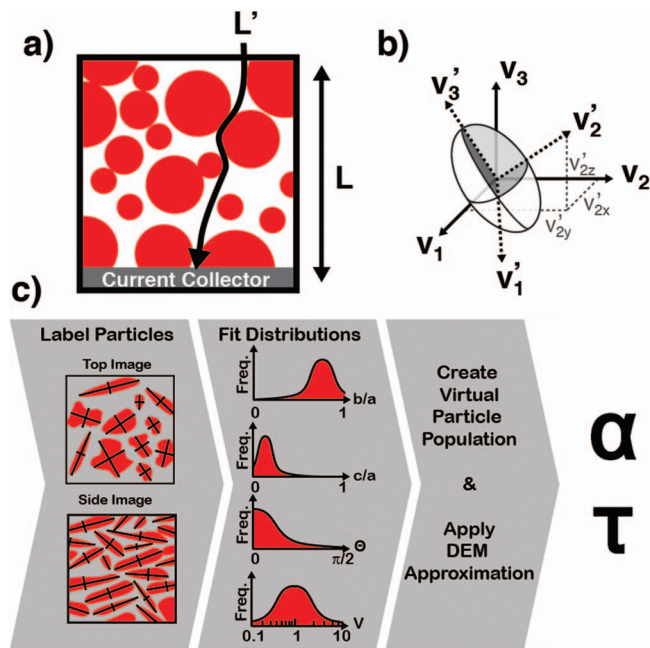
Figure 1. (a) Sketch of electrode cross-section showing the diffusion length, L', and the electrode thickness, L. (b) The coordinate system of the electrode $\{v_1, v_2, v_3\}$ and of a particle $\{v_1', v_2', v_3'\}$. The gray markings $\{v_{2x}', v_{2y}', v_{2z}'\}$ label a particle basis vector v_2 in the coordinates of the electrode. (c) Schematic workflow of the *BruggemanEstimator* software: Two microscope images are loaded into the program and the user labels the axes of several particles. These data points are used to calculate distributions of particle shape and orientation within the electrode. The DEM approximation is then applied to calculate the Bruggemann exponents $\{\alpha_x, \alpha_y, \alpha_z\}$.

We validate the accuracy of *BruggemanEstimator* for different types of particles by comparing the estimated Bruggeman exponents to values calculated by performing numerical diffusion simulations on three-dimensional microstructures obtained from both SRXTM and FIB/SEM tomography.

Theory

Differential effective medium (DEM) approximation.— The DEM approximation was introduced by Bruggeman in 1935 to describe the effective conductivity of mixed media.[12] Because diffusion and conduction are both described by the Laplace Equation $\Delta \varphi = 0$ (i.e. the *Laplace operator* $\Delta = \nabla^2$ acting on a scalar field φ), the DEM approximation can equally well be applied to understand lithium diffusion in electrolyte phase of a porous electrode.[14]

The DEM approximation considers the effective diffusivity, D_{eff}, of a material with diffusivity D_1 having discrete inclusions with diffusivity D_2 occupying a volume fraction ϕ_2. In the case of porous electrodes, the material with $D_1 = D_0$ is the liquid electrolyte and the discrete inclusions are the active particles. Because the diffusivity of the electrolyte is typically orders of magnitude larger than the diffusivity within the solid particles, we assume $D_2 = 0$ to simplify the equations. In this work, we focus on estimating the tortuosity due to the active particles and neglect the additional tortuosity that can result from inactive components such as carbon black or polymer binder. The contributions to tortuosity from these phases can be considered.[9,15]

The rationale behind the DEM approximation is as follows: if the effective diffusivity $D_{eff}(\phi_2)$ of the composite (particles and electrolyte) is known for one value of ϕ_2, then $D_{eff}(\phi_2 + \Delta\phi_2) - D_{eff}(\phi_2)$ represents the change in effective diffusivity due to the addition of a fraction $\Delta\phi_2$ of particles with D_2 at the expense of a fraction $\Delta\phi_2/(1-\phi_2)$ of the composite with $D_{eff}(\phi_2)$. For small $\Delta\phi_2$, this small change in diffusivity can be estimated by the proportionality f.[14]

$$D_{eff}(\phi_2 + \Delta\phi_2) - D_{eff}(\phi_2) \approx f \frac{\Delta\phi_2}{1 - \phi_2} \qquad [6]$$

Starting from a known diffusivity $D_{eff}(\phi_2\{1\} = 0) = D_1$ and adding particle by particle (labeled by the index i) with known proportionality $f\{i\}$ and employing Eq. 6 iteratively until the final volume fraction ϕ_2 is reached then gives an estimate for $D_{eff}(\phi_2)$. This process is known as *incremental homogenization*.[14]

To account for microstructural anisotropy introduced by shape anisotropic particles,[9] we write the direction dependent quantities as tensors and indicate them with bold letters. The proportionality f becomes the *proportionality tensor $\boldsymbol{f}$*, which depends on the shape and orientation of the active particles. It is calculated for arbitrarily shaped and oriented ellipsoids with:[14]

$$\boldsymbol{f} = (\boldsymbol{D_2} - \boldsymbol{D_{eff}}) \cdot \left[\boldsymbol{I} + \boldsymbol{A} \cdot \boldsymbol{D_{eff}}^{-1} \cdot (\boldsymbol{D_2} - \boldsymbol{D_{eff}}) \right]^{-1} \qquad [7]$$

and simplifies under the above mentioned assumption $\boldsymbol{D_2} = 0$ to:

$$\boldsymbol{f} = -\boldsymbol{D_{eff}} \cdot [\boldsymbol{I} - \boldsymbol{A}]^{-1} \qquad [8]$$

Here, $\boldsymbol{I}$ is the identity matrix and $\boldsymbol{A}$ is the *depolarization tensor*[c] containing the information about shape and orientation of a single particle i and how it contributes to the effective diffusivity. Specifically, the eigenvalues A_k of $\boldsymbol{A}$ are related to the particle shape while the eigenvectors v_k' are related to the particle orientation:[16]

$$A_k = \frac{abc}{2} \int_0^\infty \frac{dt}{(t + k^2)\sqrt{(t + a^2)(t + b^2)(t + c^2)}} \qquad [9]$$

with k being the major (a), median (b) and minor (c) axis of the ellipsoid. As shown in Appendix A, the *Bruggeman exponent tensor* $\boldsymbol{\alpha}$ for a single particle is related to the depolarization tensor via:

$$\boldsymbol{I} + \boldsymbol{\alpha} = [\boldsymbol{I} - \boldsymbol{A}]^{-1} \qquad [10]$$

We call the coordinate system of the particles (i.e. all principal axes of the ellipsoid aligned to basis vectors) base $\boldsymbol{B}$, and the coordinate system of the electrode (i.e. z-axis parallel to the electrode surface normal) base $\boldsymbol{B}'$. These coordinate systems are shown in Figure 1b. In the coordinate system of the particle (base $\boldsymbol{B}$), the depolarization tensor is a diagonal matrix:

$$\boldsymbol{A_B^B} = \mathrm{diag}(A_1, A_2, A_3) \qquad [11]$$

The orientation of the particle is expressed in the *transformation matrix* $\mathbf{T}_{\boldsymbol{B}'}^{\boldsymbol{B}}$ that is constructed by expressing the basis vectors of $\boldsymbol{B}$ in coordinates of $\boldsymbol{B}'$:

$$\mathbf{T}_{\boldsymbol{B}'}^{\boldsymbol{B}} = \begin{pmatrix} v_1' & v_2' & v_3' \end{pmatrix} \text{ with } v_i' = \begin{pmatrix} v_{ix}' \\ v_{iy}' \\ v_{iz}' \end{pmatrix} \qquad [12]$$

The Bruggeman exponent tensor in the coordinate system of the electrode (base $\boldsymbol{B}'$) can then be expressed by:

$$\boldsymbol{\alpha}_{\boldsymbol{B}'}^{\boldsymbol{B}'} = \mathbf{T}_{\boldsymbol{B}'}^{\boldsymbol{B}} \cdot \boldsymbol{\alpha}_{\boldsymbol{B}}^{\boldsymbol{B}} \cdot \left(\mathbf{T}_{\boldsymbol{B}'}^{\boldsymbol{B}} \right)^T \qquad [13]$$

To use the DEM approximation, the following two things must be known for each particle i out of a population of N particles: its shape, parameterized by $a\{i\}$, $b\{i\}$ and $c\{i\}$, and its orientation, parameterized by the two azimuth angles $\psi\{i\}$ and $\psi_2\{i\}$, and the elevation angle $\theta\{i\}$. The shape is used to calculate $\boldsymbol{\alpha}_{\boldsymbol{B}}^{\boldsymbol{B}}$ while the orientation and elevation angle are used to calculate $\mathbf{T}_{\boldsymbol{B}'}^{\boldsymbol{B}}$. While the particle volumes $V\{i\}$ are in principle required to calculate $\Delta\phi_2\{i\}$ and $\phi_2\{i\}$, they can be ignored under the conditions discussed below.

Knowing the particle shapes and orientations, the effective diffusivity tensor $\boldsymbol{D_{eff}}(\phi_2)$ is given by:

$$\frac{\boldsymbol{D_{eff}}(\phi_2)}{D_1} = \prod_{i=1}^{N} \left(\boldsymbol{I} - \frac{\Delta\phi_2\{i\}}{(1 - \phi_2\{i\})} \left(\boldsymbol{I} + \boldsymbol{\alpha}_{\boldsymbol{B}'}^{\boldsymbol{B}'}\{i\} \right) \right) \qquad [14]$$

---

[c]The term originates from electromagnetic theory.[16]

with the volume fraction contribution of the ith particle:

$$\Delta\phi_2\{i\} = (1 - \varepsilon)\frac{V\{i\}}{\sum_{j=1}^{N} V\{j\}} \qquad [15]$$

and the sum of the volume fractions of all particles up to the ith particle:

$$\phi_2\{i\} = \sum_{j=1}^{i} \Delta\phi_2\{i\} \qquad [16]$$

However, Eq. 14 violates one requirement for an effective medium approximation namely that the result should not depend on the *sequence* in which the particles are added. Specifically, the term $w\{i\} = \frac{\Delta\phi_2\{i\}}{(1-\phi_2\{i\})}$ in Eq. 14 determines the "weight" of each particle and Eq. 15 and Eq. 16 lead to a monotonous increasing $w\{i\}$ with i. In other words, the particles added last contribute most. As shown in Appendix B, this unsatisfying situation can be overcome by replacing the weighing term $w\{i\}$ above with:

$$w\{i\} = \mathrm{Ln}\left(\frac{1}{\varepsilon}\right)\frac{V\{i\}}{\sum_{j=1}^{N} V\{j\}} = \frac{\mathrm{Ln}(1/\varepsilon)}{N} \qquad [17]$$

This assumes no correlation among particle volume, shape, and orientation at the single particle level (e.g., smaller particles are not shaped differently than larger particles).

We can then write down a simplified equation for the effective diffusivity tensor:

$$\frac{\boldsymbol{D}_{eff}(\phi_2)}{D_1} = \prod_{i=1}^{N}\left(\mathbf{I} + \frac{\mathrm{Ln}(\varepsilon)}{N}\left(\mathbf{I} + \boldsymbol{\alpha}_{B'}^{B'}\{i\}\right)\right) \qquad [18]$$

As we show in Appendix D, we can reformulate this equation to calculate the effective Bruggeman exponent tensor:

$$\boldsymbol{\alpha}_{eff} = \frac{\mathrm{Ln}[\boldsymbol{D}_{eff}(\phi_2)/D_1]}{\mathrm{Ln}(\varepsilon)} - \boldsymbol{I} = \frac{1}{N}\sum_{i=1}^{N}\boldsymbol{\alpha}_{B'}\{i\} \qquad [19]$$

from which the directional tortuosities for a porous electrode can be calculated. We note the surprising result that in the considered case of no correlation between particle volume, shape, and orientation, the effective Bruggeman exponent tensor is simply the arithmetic mean of the Bruggeman exponent tensors of the individual particles. As described in Appendix E, we take advantage of this to enable a fast numerical calculation of the effective Bruggeman exponent tensor in the *BruggemanEstimator* software.

Experimental

Implementation of the software BruggemanEstimator.— The general concept of the *BruggemanEstimator* software is sketched in Figure 1c. The software is implemented in Wolfram Mathematica and leverages its rich and versatile library of interactive calculation and plotting capabilities. A Mathematica notebook containing the program and the source code is available free of charge online.[17]

Upon pressing the *Build!* button, a lookup table of Bruggeman exponents is calculated by solving Eq. 9 for a discrete set of ellipsoidal shapes. The size of the set can be chosen by the user. The interface is shown in Figure 2. The user loads two images of the electrode - a top-view (Figure 2b) and a cross-sectional view (Figure 2c) – which can be taken with an optical or scanning electron microscopy, depending on the resolution needed to visualize the active particles. Then, the user manually labels particles by dragging markers onto the images. The markers should label the two principal axes observed in the two-dimensional images (i.e. the longest and shortest axes) such that the indicated ellipse fits the particle well. We represent each particle by an ellipsoid and interpret the principal axes marked in the top view image as the major and median axes. The shorter axis in the cross-sectional image is identified as the minor ellipsoid axis while the longer axis is also identified as the major axis and is used to determine the elevation angle. Upon pressing the *Fit!* button, a modified
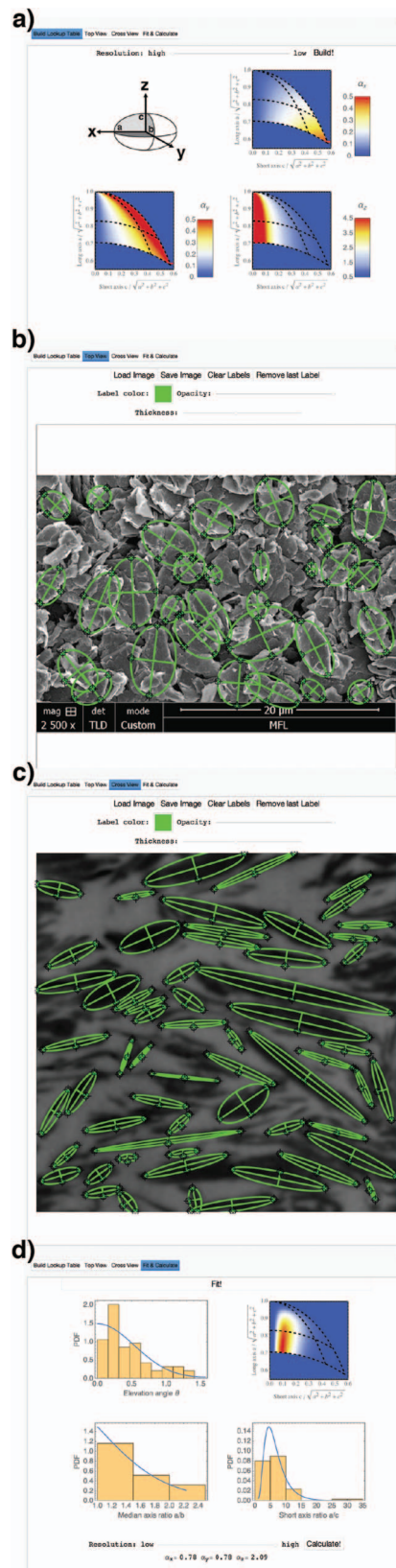
Figure 2. Screenshots of the *BruggemanEstimator* software: In the first tab (a), the lookup table for the Bruggeman exponents is calculated and displayed, in the second (b) and third (c) tabs, the top and cross-sectional images are loaded and particles are labeled. In the last tab (d), models for shape and orientation distributions are fitted to histograms calculated from the particle labeling, and the Bruggeman exponents are calculated.

lognormal distribution $\mathfrak{D}_{\mu,\sigma}$ (to account for $a > b > c$) is fitted to the axis ratios a/b and a/c, and a modified normal distribution with zero mean $\mathfrak{F}_{\sigma}$ (to account for $\theta \in [0, \pi/2]$) is fitted to the elevation angle θ. The angles ψ and ψ_2 are assumed to follow a uniform distribution $\mathfrak{A}_{0,2\pi}$. The probability density functions of all distributions are given in Appendix C. From a typical microscope image of a porous electrode, a user can reliably identify about 50–90 particles, a number which is sufficient to construct representative histograms of the particle dimensions. Finally, when the *Calculate!* Button is pressed, Eq. 52 and Eq. 46–Eq. 48 are solved and the main components $\{\alpha_x, \alpha_y, \alpha_z\}$ of the resulting effective Bruggeman exponent tensor are displayed, as shown in Figure 2d.

Electrode preparation.— Preparation of the electrodes featuring spherical $LiNi_{1/3}Mn_{1/3}Co_{1/3}O_2$ (NMC) and triaxial $LiCoO_2$ (LCO) particles, as well as SRXTM experiments and calculation of Bruggeman exponents for these electrodes is reported in Ref. 9. Graphite electrode slurries with a weight ratio of 95:5 active material (KS6 L from TIMCAL Ltd., Bodio, Switzerland) to binder (HSV900 from Arkema, Philadelphia, PA, USA) are prepared in N-methyl pyrrolidone (NMP, biotech grade from Sigma-Aldrich Chemie GmbH, Buchs, Switzerland). The ingredients are mixed for 10 min using a high-shear disperser (ULTRA-DURRAX T 10, IKA Werke GmbH, Germany), rested on a roller bench for up to 3 h to remove bubbles, and cast onto 10 µm thick copper foil with an automatic film applicator (byko-drive, Byk-Gardner GmbH, Geretsried, Germany) using a 200 µm notch bar. The films are then dried under vacuum for 8 h at 80°C and electrodes with a diameter of 13 mm are punched out with a proprietary puncher. Finally, some electrodes are compressed with a hydraulic press (CrushIR, PIKE technologies, Madison, WI, USA) with 150 bar.

FIB tomography.— To facilitate reconstruction of the 3D dataset from FIB slices, specifically the discrimination between graphite and pore-space, the pores are filled with silicone (Elastosil RT 601 A/B, Wacker Chemie AG, Munich, Germany) by vacuum infiltration.[18] In contrast to most epoxy resins, this silicone provides sufficient contrast to the graphite particles needed for data processing. After curing, the copper current collector is carefully removed from the back side of the electrode, and the exposed electrode surface is sputter-coated with a 10 nm layer of Pd/Au to improve conductivity. FIB tomography is then performed on a FEI Helios NanoLab 450S equipped with a 30 kV Ga$^+$ source. To minimize curtaining effects, the area of interest is covered by a 1 µm thick Pt layer by ion-beam induced metal deposition. By ion-milling a U-shaped trench at 64 nA, a cubic volume of $30 \times 30 \times 12$ µm^3 is excavated to expose the electrode cross-section. After polishing the cross-section with low currents, an automatic slicing and imaging routine (AutoSliceAndView G3, FEI, Hillsboro, OR, USA) is started. This software alternately mills 29 nm thick slices with the ion beam at 2.5 nA and records images at 6.4 nA and 3 kV with the electron beam using an in-lens detector in backscattered electron mode. This procedure requires about 40 sec per slice and runs overnight.

Data preprocessing.— Preprocessing of the FIB tomography data is performed entirely using the open source software Fiji:[19] First, image drift is compensated by registration using the *StackReg* Plugin in *Translation* mode.[20] In a second step, the stack of SEM images is downscaled to (29 nm)^3 isotropic voxel size. Then, the images are filtered in the frequency domain (*FFT Bandpass Filter* plugin by Joachim Walter) to remove features smaller than 3 px and larger than 100 px and suppress vertical stripes with 5% tolerance. These filtered gray-scale images are then binarized based on a threshold value that is chosen such that the resulting electrode porosity matches the porosity determined by weighing and measuring the electrode thickness. The resulting binary $340 \times 340 \times 340$ voxel dataset, representing $(9.86$ µm$)^3$, is then used as input for numerical tortuosity determination.

Table I. Bruggeman exponents of NMC, LCO, and graphite electrodes obtained from tomographic techniques and the *BruggemanEstimator* software. The deviation between the calculated and estimated values is about 10%.

Material	Technique	α_x (in-plane)	α_y (in-plane)	α_z (through-plane)
NMC	SRXTM, Ref. 9	0.54	0.53	0.57
	BruggemanEstimator	0.50	0.50	0.53
LCO	SRXTM, Ref. 9	0.63	0.65	0.83
	BruggemanEstimator	0.58	0.58	0.78
Graphite	FIB/SEM	0.79	0.95	1.87
	BruggemanEstimator	0.79	0.79	2.08

Numerical tortuosity determination.— Tortuosity of the graphite electrode is calculated by numerically solving Laplace's equation in the pore-space of the preprocessed dataset employing Dirichlet boundary conditions using commercial software (*DiffuDict* module of *GeoDict2013* from Math2Market GmbH, Kaiserslautern, Germany). Bruggeman exponents determined by FIB-SEM tomography are tabulated in Table I.

Results and Discussion

Verification of BruggemanEstimator.— SEM images of the top and cross-sections of electrodes containing spherical NMC and triaxial LCO particles are shown in Figure 3. These images are loaded into
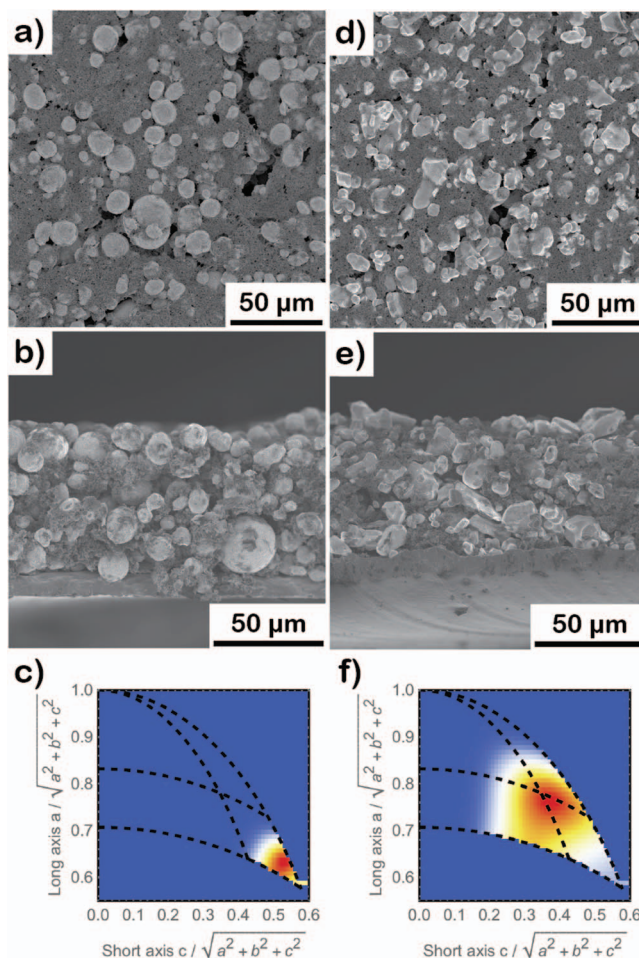

Figure 3. Top (a,d) and cross-sectional (b,e) SEM images of electrodes with spherical NMC (a-c) and triaxial LCO (d-f) particles and particle shape distributions extracted with the *BruggemanEstimator* software (c,f).
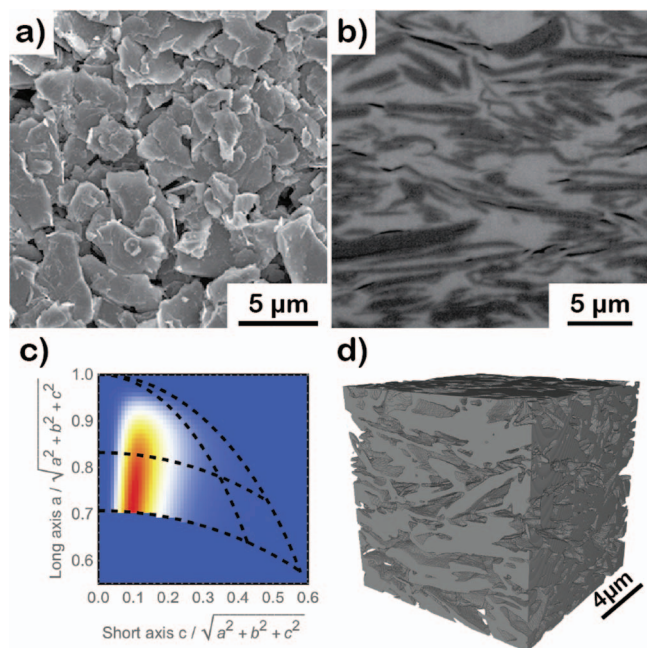
Figure 4. Scanning electron micrographs of (a) the top of a graphite electrode and (b) the cross-section through this electrode after infilling with silicone and preparation with a focused ion beam, and (c) the particle shape distribution extracted with the software *BruggemanEstimator*. (d) 3D-rendering of same electrode microstructure obtained by FIB-SEM tomography.

the software *BruggemanEstimator* and 50–90 particles are manually labeled to extract the particle shape distributions depicted in Figure 3c and 3f. The calculated Bruggeman exponents are listed in Table I. For comparison, the values calculated by numerical diffusion simulations based on SRXTM datasets reported in Ref. 9 are also given.

To showcase the versatility of the software *BruggemanEstimator*, we next investigate small platelet shaped graphite with a particle size of about 3 μm. The combination of low material contrast and small particle size makes this a challenging specimen for analysis via SRXTM. In Figure 4, top and cross-section SEM images are shown. The cross-section is prepared by focused ion beam milling of the electrode after infilling of the pores with silicone, but can also be prepared with a microtome. Again, we compare the results from the *BruggemanEstimator* software to those obtained through a tomographic technique. We perform FIB/SEM tomography on the same sample, as described in the Experimental Section. A three-dimensional rendering of the obtained electrode microstructure is shown in Figure 4d.

Table I shows that the values obtained by the *BruggemanEstimator* compare well to those obtained with the more complex and time-consuming tomography techniques. *BruggemanEstimator* thus offers a simple, fast, and accessible approach to estimate the Bruggeman exponents with an accuracy of about 10%, which is acceptable for the purpose of most tortuosity estimations.

Limitations of BruggemanEstimator.— The software *BruggemanEstimator* captures the influence of particle shape and orientation distributions on the tortuosity of porous electrodes. Since it is a manual 2D technique, there are limitations to its accuracy. The main limitation is connected to the fundamental problem of capturing the correct three dimensional shape distribution of a particle population from two-dimensional images. Indeed, there are subtle differences whether a "fracture" cross-section that leaves each particle in tact (such as in Figure 3b and 3e) or a "sharp" FIB cross-section that cuts the particles apart (such as in Figure 4b). In the FIB case, the cross-section through the electrode does not necessarily go through the center of each particle and is not perfectly aligned to the principal

axes of each particle, but rather sections the particles randomly. Thus, the axis ratios that are extracted from the manually placed labels are not exactly the ratios of the principal axes and the extracted elevation angles might not be perfectly accurate. However, for the purpose of quickly estimating the particle shape and orientation distributions, this can be tolerated as long as cases with extreme aspect ratios, such as fiber-like materials, are avoided.

While the trend in commercial battery manufacturing is to minimize the amount of conductive additives and polymer binder, if large amounts of these additives are homogeneously distributed in the pore space between the micrometer scale active particles, the tortuosity stemming from the additives can be multiplied to the tortuosity calculated by *BruggemanEstimation* to give the total tortuosity.[15,22]

In the interest of usability, the software *BruggemanEstimation* imposes some assumptions on the statistical distribution of particle shape and orientation and might therefore not always provide the optimal results for exotic situations such as electrodes with graded porosity or electrodes manufactured from a blend of two types of particles. Users are invited to adapt the freely available code to deal with these more complex situations.

Some limitations of the DEM approximation can be identified: The DEM approximation will overestimate the effective transport parameters for ultra low porosity electrodes with closed porosity, because the DEM approximation is not capable of predicting a percolation threshold.[14] The electrochemical response of strongly inhomogeneous electrodes may not be determined by the average electrode microstructure as quantified by DEM, but may be carried by ionically well connected parts of the electrode while other parts are electrochemically inactive as discussed by Harris and Lu.[23] Analysis of such situations requires the use of full three-dimensional techniques such as SRXTM and FIB/SEM tomography where inhomogeneity and closed porosity can be studied in detail.

Conclusions

We proved that the Differential Effective Medium approximation simplifies considerably under conditions typically met by porous battery electrodes where it becomes the arithmetic mean of the Bruggeman exponent tensors of individual particles.

We developed the *BruggemanEstimator* software and offer it open source to the research community for estimating the Bruggeman exponents of a porous electrode. The estimate is based on the extraction of particle shape and orientation from two microscope images taken of the porous electrode. By fitting mathematical models to the extracted particle shape and orientation distributions, the software allows quick and reliable estimates of the effective Bruggeman exponent tensor of the electrode. We validate the accuracy of the results against values calculated from three-dimensional tomography datasets and show that it lies in the range of 10%.

BruggemanEstimator offers the research community the possibility to quickly estimate from actual electrode data obtained from low-cost and available techniques, values for tortuosity to be used in Newman model based effective transport simulations. The influence of new active particle shapes or novel manufacturing techniques, which can affect particle alignment in the electrode, can be quantified and used to better understand battery performance and make informed decisions about future research and development directions.

Appendix A: The Bruggeman Exponent Tensor α

Here we show how the DEM approximation is related to the Bruggeman relation. Eq. 6 can be rewritten to:

$$\Delta \boldsymbol{D}_{eff} \approx -\boldsymbol{D}_{eff} \cdot [\boldsymbol{I} - \boldsymbol{A}]^{-1} \frac{\Delta \phi_2}{1 - \phi_2} \qquad [20]$$

Under the assumption of identical particles (i.e. constant $\boldsymbol{A}$), in the limit of $\Delta\phi_2 \to 0$ Eq. 20 becomes the differential equation

$$\frac{\partial \boldsymbol{D}_{eff}}{\boldsymbol{D}_{eff}} = -[\boldsymbol{I} - \boldsymbol{A}]^{-1} \frac{\partial \phi_2}{1 - \phi_2} \qquad [21]$$

After integration with $\boldsymbol{D}_{eff}(\phi_2 = 0) = D_1$, it follows from Eq. 1 and Eq. 5 that

$$\frac{\boldsymbol{D}_{eff}}{D_1} = \varepsilon^{I+\alpha} = \varepsilon^{[I-A]^{-1}}. \qquad [22]$$

Thus

$$\boldsymbol{I} + \boldsymbol{\alpha} = [\boldsymbol{I} - \boldsymbol{A}]^{-1} \qquad [23]$$

Next, we show that we can first calculate the Bruggeman exponent tensor of the *unrotated* particles (in the particle coordinate system) and then calculate the Bruggeman exponent tensors of the *rotated* particles in the coordinate system of the electrode. This allows precalculation of Eq. 23.

To transform the depolarization tensor $\boldsymbol{A}$ from the particle coordinate system (base $\boldsymbol{B}$) to the electrode coordinate system (base $\boldsymbol{B}'$), we use:

$$\boldsymbol{A}_{\boldsymbol{B}'}^{\boldsymbol{B}'} = \mathbf{T}_{\boldsymbol{B}'}^{\boldsymbol{B}} \cdot \boldsymbol{A}_{\boldsymbol{B}}^{\boldsymbol{B}} \cdot \left(\mathbf{T}_{\boldsymbol{B}'}^{\boldsymbol{B}}\right)^T \qquad [24]$$

Substituting Eq. 24 into the right hand side of Eq. 23:

$$\left[\boldsymbol{I} - \mathbf{T}_{\boldsymbol{B}'}^{\boldsymbol{B}} \cdot \boldsymbol{A}_{\boldsymbol{B}}^{\boldsymbol{B}} \cdot \left(\mathbf{T}_{\boldsymbol{B}'}^{\boldsymbol{B}}\right)^T\right]^{-1} - \boldsymbol{I} = \mathbf{T}_{\boldsymbol{B}'}^{\boldsymbol{B}} \cdot \left(\left[\boldsymbol{I} - \boldsymbol{A}_{\boldsymbol{B}}^{\boldsymbol{B}}\right]^{-1} - \boldsymbol{I}\right) \cdot \left(\mathbf{T}_{\boldsymbol{B}'}^{\boldsymbol{B}}\right)^T \qquad [25]$$

we find that the coordinate transformation for the Bruggeman exponent tensor is:

$$\boldsymbol{\alpha}_{\boldsymbol{B}'} = \mathbf{T}_{\boldsymbol{B}'}^{\boldsymbol{B}} \cdot \boldsymbol{\alpha}_{\boldsymbol{B}} \cdot \left(\mathbf{T}_{\boldsymbol{B}'}^{\boldsymbol{B}}\right)^T \qquad [26]$$

Appendix B: Redefinition of the Weighing Function $w\{i\}$

For identical particles $V\{i\} = V_0$, the weighing function becomes $w\{i\} = \frac{\Delta\phi_2\{i\}}{(1-\phi_2\{i\})} = \frac{1}{\frac{N}{(1-\varepsilon)}-i}$. It is easily seen that particles added later (large i) will have larger weights, which violates the discussed criterion for an effective medium approximation. To find a better weighing function, we leverage a further requirement for an effective medium approximation: Namely, for a population of identical particles the approximation should yield the same result as the single particle. Specifically, Eq. 14 with constant $\boldsymbol{\alpha}$ should give the same result as Eq. 1 and Eq. 5 for the same $\boldsymbol{\alpha}$.

We utilize the limit definition of the exponential function

$$e^x = \lim_{N\to\infty}\left(1 + \frac{x}{N}\right)^N \qquad [27]$$

and the identity

$$a^x = e^{x \cdot Ln(a)} \qquad [28]$$

to write

$$\varepsilon^{1+\alpha} = \lim_{N\to\infty}\prod_{i=1}^{N}\left(1 + \frac{Ln(\varepsilon)}{N}(1+\alpha)\right) \qquad [29]$$

For identical particles, we can compare Eq. 29 to Eq. 14:

$$\frac{\boldsymbol{D}_{eff}(\phi_2)}{D_1} = \prod_{i=1}^{N}\left(\mathbf{I} - \frac{\Delta\phi_2\{i\}}{(1-\phi_2\{i\})}\left(\mathbf{I} + \boldsymbol{\alpha}_{\boldsymbol{B}'}^{\boldsymbol{B}'}\{i\}\right)\right) \qquad [30]$$

Identifying and comparing the weighing terms and using the Riemann sum:

$$\lim_{N\to\infty}\sum_{i=1}^{N}\frac{\Delta\phi_2\{i\}}{(1-\phi_2\{i\})} = \lim_{N\to\infty}\sum_{i=1}^{N}\frac{1}{N}\frac{1}{\frac{1}{1-\varepsilon}-\frac{i}{N}}$$

$$= \int_0^1 \frac{1}{\frac{1}{1-\varepsilon}-t}dt = -Ln\left(\frac{1}{1-\varepsilon}-t\right)\Big|_0^1 = Ln\left(\frac{1}{\varepsilon}\right) \qquad [31]$$

yields:

$$\sum_{i=1}^{N} w\{i\} = \sum_{i=1}^{N}\frac{\Delta\phi_2\{i\}}{(1-\phi_2\{i\})} = \sum_{i=1}^{N}\frac{-Ln(\varepsilon)}{N} = Ln\left(\frac{1}{\varepsilon}\right) \qquad [32]$$

Any weighing function $w\{i\}$ for an effective medium approximation has to fulfill Eq. 32.

Appendix C: Probability Density Functions

Uniform Distribution

$$PDF[\mathfrak{A}_{a,b}](x) = \begin{cases} \dfrac{1}{b-a} & a \le x \le b \\ 0 & elsewhere \end{cases} \qquad [33]$$

Normal Distribution

$$PDF[\mathfrak{N}_{\mu,\sigma}](x) = \frac{1}{\sqrt{2\pi}\sigma}e^{-\frac{(x-\mu)^2}{2\sigma^2}} \qquad [34]$$

Lognormal Distribution

$$PDF[\mathfrak{L}_{\mu,\sigma}](x) = \begin{cases} \dfrac{1}{\sqrt{2\pi}\cdot x \cdot \sigma}e^{\frac{(Ln(x)-\mu)^2}{2\sigma^2}} & x > 0 \\ 0 & x \le 0 \end{cases} \qquad [35]$$

Axis Ratio Distribution

$$PDF[\mathfrak{D}_{\mu,\sigma}](x) = \begin{cases} \mathfrak{L}_{\mu,\sigma}(x) + \dfrac{1}{x^2}\cdot \mathfrak{L}_{\mu,\sigma}\left(1/x\right) & x \ge 1 \\ 0 & x < 1 \end{cases} \qquad [36]$$

Elevation Angle Distribution

$$PDF[\mathfrak{F}_{\sigma}](x) = \begin{cases} 2\dfrac{\mathfrak{N}_{0,\sigma}(x) + \mathfrak{N}_{0,\sigma}(\pi - x)}{Erf\left(\dfrac{\pi}{\sqrt{2}\sigma}\right)} & 0 \le x \le \pi/2 \\ 0 & elsewhere \end{cases} \qquad [37]$$

Euler Angle Distribution

$$PDF[\mathfrak{E}_{\sigma}](x) = \begin{cases} \dfrac{x}{\sigma^2}e^{-\frac{x^2}{2\sigma^2}} & x \ge 0 \\ 0 & x < 0 \end{cases} \qquad [38]$$

Appendix D: Arithmetic Mean

To prove the simplification shown in Eq. 19, we make use of the substitution:

$$\boldsymbol{\beta}\{i\} = Ln(\varepsilon)(\boldsymbol{I} + \boldsymbol{\alpha}_{\boldsymbol{B}'}\{i\}) \qquad [39]$$

and employ the series expansion of the natural logarithm:

$$Ln(1+x) = \sum_{k=1}^{\infty}(-1)^{k+1}\frac{x^k}{k} = x - \frac{x^2}{2} + \frac{x^3}{3} - \frac{x^4}{4} + \dots \qquad [40]$$

After inserting this expansion, we drop quadratic and higher order terms. This is justified because the higher order terms are weighted by N^{-2}, N^{-3}, ... and thus become arbitrarily small for large N.

$$\begin{aligned}\boldsymbol{\alpha}_{eff} &= \frac{Ln\left[\boldsymbol{D}_{eff}(\phi_2)/D_1\right]}{Ln(\varepsilon)} - \boldsymbol{I} = \frac{Ln\left[\prod_{i=1}^{N}\left(\boldsymbol{I} + \frac{Ln(\varepsilon)}{N}(\boldsymbol{I} + \boldsymbol{\alpha}_{\boldsymbol{B}'}\{i\})\right)\right]}{Ln(\varepsilon)} - \boldsymbol{I} \\ &= \frac{Ln\left[\prod_{i=1}^{N}\left(\boldsymbol{I} + \frac{\boldsymbol{\beta}\{i\}}{N}\right)\right]}{Ln(\varepsilon)} - \boldsymbol{I} = \frac{\sum_{i=1}^{N}Ln\left[\boldsymbol{I} + \frac{\boldsymbol{\beta}\{i\}}{N}\right]}{Ln(\varepsilon)} - \boldsymbol{I} \\ &= \frac{\sum_{i=1}^{N}\left(\frac{\boldsymbol{\beta}\{i\}}{N} - \frac{\boldsymbol{\beta}\{i\}^2}{2N^2} + \frac{\boldsymbol{\beta}\{i\}^3}{3N^3} - \dots\right)}{Ln(\varepsilon)} - \boldsymbol{I} \approx \frac{\sum_{i=1}^{N}\boldsymbol{\beta}\{i\}}{NLn(\varepsilon)} - \boldsymbol{I} \\ &= \frac{\sum_{i=1}^{N}Ln(\varepsilon)(\boldsymbol{I} + \boldsymbol{\alpha}_{\boldsymbol{B}'}\{i\})}{NLn(\varepsilon)} - \boldsymbol{I} = \frac{1}{N}\sum_{i=1}^{N}\boldsymbol{\alpha}_{\boldsymbol{B}'}\{i\} = \langle\boldsymbol{\alpha}_{\boldsymbol{B}'}\rangle \end{aligned} \qquad [41]$$

Thus, the effective Bruggeman exponent tensor calculated by the DEM approximation is equal to the arithmetic mean of the individual particle Bruggeman exponent tensors.

Appendix E: Efficient Calculation

The straightforward approach to calculate the effective Bruggeman exponent tensor would be to draw N virtual particles from a population with shape and orientation distributions, and then apply Eq. 19. This is computationally expensive because the integral in Eq. 9 must then be solved N times.

Alternatively, the calculation of the integral can be performed once for a discrete set of shapes and the results combined with a discrete set of orientations according to their respective probabilities. Because, as discussed above, we ignore any correlation between shape and orientation on a single particle level, we can decouple these individual calculations. Furthermore, we can split the transformation matrix into three consecutive rotations about the *Euler angles* α, β and γ:

$$\mathbf{T}_{\boldsymbol{B}'}^{\boldsymbol{B}} = \boldsymbol{R}_z(\gamma) \cdot \boldsymbol{R}_x(\beta) \cdot \boldsymbol{R}_z(\alpha) \qquad [42]$$

with the rotation matrices:

$$\boldsymbol{R}_z(x) = \begin{pmatrix} Cos(x) & -Sin(x) & 0 \\ Sin(x) & Cos(x) & 0 \\ 0 & 0 & 1 \end{pmatrix} \qquad [43]$$

$$\boldsymbol{R}_x(x) = \begin{pmatrix} 1 & 0 & 0 \\ 0 & Cos(x) & -Sin(x) \\ 0 & Sin(x) & Cos(x) \end{pmatrix} \qquad [44]$$

To guarantee that the eigenvectors of the resulting transformation matrices provide the required distributions for ψ, θ, and ψ_2, α and γ are chosen uniformly distributed ($\mathfrak{A}_{0,2\pi}$) while β follows the square root of the exponential distribution, which we call the Euler angle distribution ($\mathfrak{E}_\sigma$).[21]

With this, we can perform the calculations consecutively:

$$W = \sum_{\frac{a}{b}=1}^{\infty} \sum_{\frac{a}{c}=1}^{\infty} PMF[\tilde{\mathfrak{D}}_{\mu_{a/b},\sigma_{a/b}}]\{a/b\} \cdot PMF[\tilde{\mathfrak{D}}_{\mu_{a/c},\sigma_{a/c}}]\{a/c\} \cdot \boldsymbol{\alpha_B} \qquad [45]$$

$$Q = \sum_{\alpha=0}^{2\pi} PMF[\tilde{\mathfrak{A}}_{0,2\pi}]\{\alpha\} \cdot \boldsymbol{R_z}(\alpha) \cdot W \cdot \boldsymbol{R_z}(\alpha)^T \qquad [46]$$

$$R = \sum_{\beta=0}^{\pi/2} PMF[\tilde{\mathfrak{E}}_{\sigma_\theta}]\{\beta\} \cdot \boldsymbol{R_x}(\beta) \cdot Q \cdot \boldsymbol{R_x}(\beta)^T \qquad [47]$$

$$\boldsymbol{\alpha_{eff}} = \sum_{\gamma=0}^{2\pi} PMF[\tilde{\mathfrak{A}}_{0,2\pi}]\{\gamma\} \cdot \boldsymbol{R_z}(\gamma) \cdot R \cdot \boldsymbol{R_z}(\gamma)^T \qquad [48]$$

where the probability mass functions (PMFs) of the corresponding *discrete* distributions fulfill:

$$\sum_i PMF[\tilde{\mathfrak{D}}_{\mu,\sigma}]\{i\} = \sum_i PMF[\tilde{\mathfrak{E}}_\sigma]\{i\} = \sum_i PMF[\tilde{\mathfrak{A}}_{a,b}]\{i\} = 1 \qquad [49]$$

Since the infinite sums in Eq. 45 are not well suited for numerical implementation, we employ the coordinate transformation:

$$\{x, y\} = \left\{ \frac{c}{\sqrt{a^2 + b^2 + c^2}}, \frac{a}{\sqrt{a^2 + b^2 + c^2}} \right\} \qquad [50]$$

with the Jacobian determinant:

$$|J| = \left| \frac{\partial \{a/b, a/c\}}{\partial \{x, y\}} \right| = \frac{y}{x^2(1 - x^2 - y^2)^{3/2}} \qquad [51]$$

under which the calculation transforms to:

$$W = \sum_{\{x,y\}\in\text{Ellipsoid}} PMF[\tilde{\mathfrak{D}}_{\mu_{a/b},\sigma_{a/b}}]\left\{ \frac{y}{\sqrt{1 - x^2 - y^2}} \right\} \cdot PMF[\tilde{\mathfrak{D}}_{\mu_{a/c},\sigma_{a/c}}]\{y/x\} \cdot |J| \cdot \boldsymbol{\alpha_B}$$
$$[52]$$

in the now finite coordinate range:

$$\{x, y\} \in \text{Ellipsoid} = \left\{ (x, y) | 0 \le x \le \sqrt{1 - x^2 - y^2} \le y \le 1 \right\} \qquad [53]$$

Appendix F: List of Symbols

ε	Porosity
$\boldsymbol{\tau}$	Tortuosity
α, $\boldsymbol{\alpha}$	Bruggeman exponent (tensor)
D	Diffusivity
κ	Conductivity
L	Transport length
r	Displacement
A	Area
t	Time
d	Dimension
ϕ	Volume fraction
$\boldsymbol{A}$	Depolarization tensor
$\boldsymbol{I}$	Identity matrix
a, b, c	Major, median, and minor ellipsoid axes
$\boldsymbol{T}$	Transformation matrix
V	Volume
υ	Vector
w	Weighing factor
ψ	Azimuth angle
θ	Elevation angle
α, β, γ	Euler angles

References

1. J. Newman and K. E. Thomas-Alyea, *Electrochemical Systems*, p. 672, John Wiley & Sons, New York (2004).
2. A. Einstein, "Über die von der molekularkinetischen Theorie der Wärme geforderte Bewegung von in ruhenden Flüssigkeiten suspendierten Teilchen," *Ann. Phys.* **322**, 549 (1905).
3. M. von Smoluchowski, "Zur kinetischen Theorie der Brownschen Molekularbewegung und der Suspensionen," *Ann. Phys.* **326**, 756 (1906).
4. N. Epstein, "On Tortuosity and the Tortuosity Factor in Flow and Diffusion through Porous Media," *Chem. Eng. Sci.* **44**, 777 (1989).
5. I. V. Thorat, D. E. Stephenson, N. A. Zacharias, K. Zaghib, J. N. Harb, and D. R. Wheeler, "Quantifying Tortuosity in Porous Li-Ion Battery Materials," *J. Power Sources* **188**, 592 (2009).
6. P. Arora, M. Doyle, A. S. Gozdz, R. E. White, and J. Newman, "Comparison Between Computer Simulations and Experimental Data for High-Rate Discharges of Plastic Lithium-Ion Batteries." *J. Power Sources* **88**, 219 (2000).
7. D. Kehrwald, P. R. Shearing, N. P. Brandon, P. K. Sinha, and S. J. Harris, "Local Tortuosity Inhomogeneities in a Lithium Battery Composite Electrode," *J. Electrochem. Soc.* **158**, A1393 (2011).
8. T. Hutzenlaub, A. Asthana, J. Becker, D. R. Wheeler, R. Zengerle, and S. Thiele, "FIB/SEM-Based Calculation of Tortuosity in a Porous LiCoO2 Cathode for a Li-Ion Battery," *Electrochem. commun.* **27**, 77 (2013).
9. M. Ebner, D.-W. Chung, R. E. García, and V. Wood, "Tortuosity Anisotropy in Lithium-Ion Battery Electrodes," *Adv. Energy Mater.* **4**, 1614 (2014).
10. M. Ebner, F. Geldmacher, F. Marone, M. Stampanoni, and V. Wood, "X-Ray Tomography of Porous, Transition Metal Oxide Based Lithium Ion Battery Electrodes," *Adv. Energy Mater.* **3**, 845 (2013).
11. S. J. Harris and P. Lu, "Effects of Inhomogeneities-Nanoscale to Mesoscale-on the Durability of Li-Ion Batteries," *J. Phys. Chem. C* **117**, 6481 (2013).
12. D. A. G. Bruggeman, "Berechnung verschiedener physikalischer Konstanten von heterogenen Substanzen. I. Dielektrizitätskonstanten und Leitfähigkeiten der Mischkörper aus isotropen Substanzen," *Ann. Phys.* **416**, 636 (1935).
13. D.-W. Chung, M. Ebner, D. R. Ely, V. Wood, and R. E. García, "Validity of the Bruggeman Relation for Porous Electrodes," *Model. Simul. Mater. Sci. Eng.* **21**, 074009 (2013).
14. S. Torquato, *Random Heterogeneous Materials: Microstructure and Macroscopic Properties*, p. 301, Springer, Berlin (2002).
15. L. Zielke, T. Hutzenlaub, D. R. Wheeler, I. Manke, T. Arlt, N. Paust, R. Zengerle, and S. Thiele, "A Combination of X-Ray Tomography and Carbon Binder Modeling: Reconstructing the Three Phases of LiCoO2 Li-Ion Battery Cathodes," *Adv. Energy Mater.* **4** 1301617 (2014).
16. J. A. Stratton, *Electromagnetic Theory*, p. 211, John Wiley & Sons, New York (1941).
17. M. Ebner and V. Wood, *BruggemanEstimator* (2014) (available at https://lne.ee.ethz.ch/en/more-information/battery-microstructure-project.html).
18. M. Ender, J. Joos, T. Carraro, and E. Ivers-Tiffee, "Quantitative Characterization of LiFePO4 Cathodes Reconstructed by FIB/SEM Tomography," *J. Electrochem. Soc.* **159**, A972 (2012).
19. J. Schindelin, I. Arganda-Carreras, E. Frise, V. Kaynig, M. Longair, T. Pietzsch, S. Preibisch, C. Rueden, S. Saalfeld, B. Schmid, J.-Y. Tinevez, D. J. White, V. Hartenstein, K. Eliceiri, P. Tomancak, and A. Cardona, "Fiji: An Open-Source Platform for Biological-Image Analysis," *Nat. Methods* **9**, 676 (2012).
20. P. Thévenaz, U. E. Ruttimann, and M. Unser, "A Pyramid Approach to Subpixel Registration based on Intensity," *IEEE Trans. Image Process.* **7**, 27 (1998).
21. G. E. P. Box and M. E. Muller, "A Note on the Generation of Random Normal Deviates," *Ann. Math. Stat.* **29**, 610 (1958).
22. B. Vijayaraghavan, D. R. Ely, Y.-M. Chiang, R. García-García, and R. E. García, "An Analytical Method to Determine Tortuosity in Rechargeable Battery Electrodes," *J. Electrochem. Soc.* **159**, A548 (2012).
23. J. Harris and P. Lu, "Effects of Inhomogeneities-Nanoscale to Mesoscale-on the Durability of Li-Ion Batteries," *J. Phys. Chem. C* **13**, 6481 (2013).